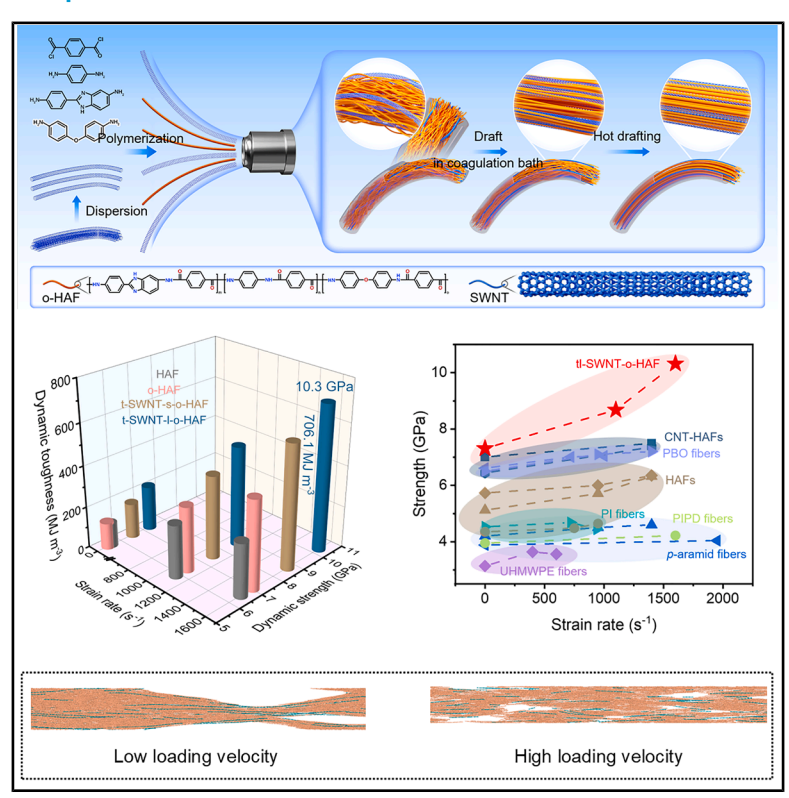
# Aramid fibers with dynamic strength up to 10 GPa and dynamic toughness up to 700 MJ m<sup>-3</sup>

#### **Graphical abstract**



#### **Highlights**

- High-strength and high-toughness aramid fibers were fabricated
- The orientation of carbon nanotubes was regulated by introducing a flexible monomer
- The excellent performance is attributed to the remarkable breakage of aramid chains

#### **Authors**

Jiajun Luo, Xudong Lei, Xiangzheng Jia, ..., Kun Jiao, Zhenfei Gao, Jin Zhang

#### Correspondence

enlaigao@whu.edu.cn (E.G.), wuxianqian@imech.ac.cn (X.W.), jiaokun-cnc@pku.edu.cn (K.J.), gaozf-cnc@pku.edu.cn (Z.G.), jinzhang@pku.edu.cn (J.Z.)

#### In brief

Ultra-high dynamic strength and toughness are crucial for fibrous materials in impact-protective applications. This study developed a strategy that regulates the orientation of carbon nanotubes within fibers to fabricate ultra-strong aramid fibers. These aligned carbon nanotubes can optimize the hierarchical structures of fibers, inducing inhibited slippage and thus remarkable breakage of aramid chains under high-speed impacts. These findings provide a feasible route for the preparation of carbon nanotube composites and high-strength and hightoughness fibers.



Luo et al., 2026, Matter 9, 102496 January 7, 2026 © 2025 Elsevier Inc. All rights are reserved, including those for text and data mining, Al training, and similar technologies. https://doi.org/10.1016/j.matt.2025.102496



Please cite this article in press as: Luo et al., Aramid fibers with dynamic strength up to 10 GPa and dynamic toughness up to 700 MJ m<sup>-3</sup>, Matter (2025), https://doi.org/10.1016/j.matt.2025.102496

## **Matter**



#### **Article**

# Aramid fibers with dynamic strength up to 10 GPa and dynamic toughness up to 700 MJ m<sup>-3</sup>

Jiajun Luo,<sup>1,2,3,8</sup> Xudong Lei,<sup>4,5,8</sup> Xiangzheng Jia,<sup>6,8</sup> Mengdie Li,<sup>1,2,8</sup> Dan Yan,<sup>2</sup> Jin Li,<sup>3</sup> Ziyi Zhang,<sup>2,3</sup> Hongbo Dai,<sup>2,3</sup> Chun Li,<sup>3</sup> Wanli Zhou,<sup>7</sup> Zuocheng Hu,<sup>2,3</sup> Xiangyang Li,<sup>2,3</sup> Shichen Xu,<sup>2</sup> Jiankun Huang,<sup>2</sup> Lianming Tong,<sup>1,2</sup> Enlai Gao,<sup>6,\*</sup> Xianqian Wu,<sup>4,5,\*</sup> Kun Jiao,<sup>2,3,\*</sup> Zhenfei Gao,<sup>3,\*</sup> and Jin Zhang<sup>1,2,3,9,\*</sup>

https://doi.org/10.1016/j.matt.2025.102496

PROGRESS AND POTENTIAL Ultra-high dynamic strength and toughness are crucial for fibrous materials in impact-protective applications. However, the trade-off between strength and toughness is a persistent challenge in materials science. Achieving simultaneous breakthroughs in both properties demands innovative fabrication strategies. Polymer chains tend to slip during loading, which undermines the effective utilization of their high intrinsic mechanical properties, thereby limiting the strength and toughness of polymer fibers. To address this issue, we developed an effective strategy that regulates the orientation of carbon nanotubes within fibers to inhibit chain slippage. Carbon nanotubes and aramid chains were molecularly engineered to achieve compatibility, while multi-stage drafting was designed for the alignment of both carbon nanotubes and aramid chains to optimize the hierarchical structures of fibers. Such optimization of hierarchical structures improves the interfacial interactions and enhances load transfer efficiency, inducing inhibited slippage and thus remarkable breakage of aramid chains under high-speed impacts. Based on this strategy, we fabricated aramid fibers with a dynamic strength up to 10 GPa and dynamic toughness up to 700 MJ m<sup>-3</sup>. Fabrics woven from these fibers also exhibit superior anti-ballistic impact performance, shedding light on practical applications of these fibers. These findings provide fresh insights into the design of high-performance fibrous materials.

#### **SUMMARY**

Ultra-high dynamic strength and toughness are crucial for fibrous materials in impact-protective applications. However, the trade-off between strength and toughness is a persistent challenge in materials science. Herein, by regulating the orientation of long carbon nanotubes within fibers, we fabricated carbon nanotube/heterocyclic aramid composite fibers with a dynamic strength of 10.3 GPa and a dynamic toughness of 706.1 MJ m<sup>-3</sup>. The ultra-high dynamic performance is attributed to the inhibited slippage and thus remarkable breakage of polymer chains during the high-strain-rate loading process; these behaviors are due to the improved alignment of polymer chains, reduced porosity, and thus enhanced interfacial interactions and load transfer efficiency therein induced by aligned long carbon nanotubes and multi-stage drafting. This work provides a fresh understanding and a feasible route for utilizing the intrinsic mechanical performance of polymer chains at the macroscale.

<sup>&</sup>lt;sup>1</sup>School of Advanced Materials, Peking University Shenzhen Graduate School, Shenzhen 518055, China

<sup>&</sup>lt;sup>2</sup>Beijing National Laboratory for Molecular Sciences, School of Materials Science and Engineering, College of Chemistry and Molecular Engineering, Academy for Advanced Interdisciplinary Studies, Beijing Science and Engineering Center for Nanocarbons, Peking University, Beijing 100871, China

<sup>&</sup>lt;sup>3</sup>Beijing Graphene Institute, Beijing 100095, China

<sup>&</sup>lt;sup>4</sup>Institute of Mechanics, Chinese Academy of Sciences, Beijing 100190, China

<sup>&</sup>lt;sup>5</sup>School of Engineering Science, University of Chinese Academy of Sciences, Beijing 100049, China

<sup>&</sup>lt;sup>6</sup>Department of Engineering Mechanics, School of Civil Engineering, Wuhan University, Wuhan 430072, China

<sup>&</sup>lt;sup>7</sup>China Bluestar Chengrand Chemical Co., Ltd, Chengdu 611430, China

<sup>8</sup>These authors contributed equally

<sup>&</sup>lt;sup>9</sup>Lead contact

<sup>\*</sup>Correspondence: enlaigao@whu.edu.cn (E.G.), wuxianqian@imech.ac.cn (X.W.), jiaokun-cnc@pku.edu.cn (K.J.), gaozf-cnc@pku.edu.cn (Z.G.), jinzhang@pku.edu.cn (J.Z.)





#### **INTRODUCTION**

Dynamic strength and toughness, which are conventionally defined as the mechanical properties measured at strain rates exceeding 10<sup>2</sup> s<sup>-1</sup>, are crucial for fibrous materials in impactprotective applications, including bulletproofing armors, vehicles, and aircraft. 1-4 Due to the high intrinsic mechanical properties and flexibility of polymer chains, synthetic high-performance polymer fibers, such as aramid fibers and ultra-high-molecular-weight polyethylene (UHMWPE) fibers, play an important role in modern industries. 5-7 However, polymer chains within these fibers tend to slip during loading due to low alignment, high porosity, and weak interfacial interactions.8-10 These behaviors undermine the effective utilization of the high intrinsic mechanical properties of individual polymer chains, thereby limiting the strength and toughness of these fibers. Furthermore, the trade-off between strength and toughness is a persistent challenge in material science. 11,12 To solve these issues, various approaches have been developed, including modification of polymer chains, 13,14 addition of reinforcements, 15,16 and optimization of assembly structures. 17,18 Despite a few achievements made in the performance improvement, the dynamic strength (<8 GPa) and dynamic toughness (<300 MJ m<sup>-3</sup>) of the obtained polymer fibers still remain far below their ideal values, indicating that there is plenty of room for improving their strength and toughness. 3,19,20

Carbon nanotubes (CNTs), with an intrinsic strength exceeding 100 GPa and a one-dimensional linear structure, <sup>21–23</sup> have been considered ideal reinforcements. <sup>24–31</sup> Previous studies found that the addition of CNTs can facilitate efficient load transfer, <sup>32,33</sup> inhibit crack propagation, <sup>34</sup> and act as templates to promote the alignment of surrounding polymer chains, <sup>35</sup> thereby enhancing the mechanical properties of polymer fibers. <sup>36–38</sup> Theoretically, long CNTs hold great potential to improve the mechanical properties of polymer fibers compared to short CNTs. <sup>20,39</sup> However, as the length of CNTs increases, they tend to bend and even entangle. <sup>8,40</sup> This issue hinders the uniform dispersion and alignment of long CNTs within polymer matrices. <sup>41</sup> Therefore, achieving uniform dispersion and alignment of long CNTs within polymer fibers for performance breakthrough remains a major challenge.

We developed a strategy that regulates the orientation of long CNTs within fibers to fabricate ultra-strong ether-group heterocyclic aramid fibers (HAFs) with a small addition of treated long single-walled CNTs (tl-SWNTs), named tl-SWNT-o-HAFs (Figure 1A). First, we did molecular engineering of building blocks, i.e., SWNTs and heterocyclic aramid chains. SWNTs were modified for uniform dispersion, and heterocyclic aramid chains were engineered to improve the chain flexibility by introducing a flexible asymmetric diamine (4,4'-diaminodiphenyl ether [ODA]). Second, multi-stage drafting was applied to fabricate the wet-spun fibers using spinning dope from the in situ polymerization of the SWNTs and heterocyclic aramid monomers. The draft ratio in the first-stage drafting in coagulation bath is significantly increased due to the improved chain flexibility. Such an increased draft ratio promotes the alignment of tl-SWNTs (Figure 1B). During the second-stage hot drafting, the tl-SWNTs act as templates to promote the alignment of the surrounding ether-group heterocyclic aramid chains and reduce

the porosity. Such optimization of hierarchical structures improves the interfacial interactions and enhances load transfer efficiency, inducing inhibited slippage and thus remarkable breakage of heterocyclic aramid chains under high-speed impacts. Consequently, the resultant fibers possess a dynamic strength of 10.3  $\pm$  0.6 GPa and a dynamic toughness of 706.1  $\pm$  46.4 MJ m $^{-3}$  (Figures 1C and 1D). Fabrics woven from mass-produced tl-SWNT-o-HAFs also exhibit superior anti-ballistic impact performance (Figures 1E and S1), shedding light on practical applications of these fibers.

#### **RESULTS**

#### **Fabrication and structure**

We used a two-step method to engineer pristine long singlewalled CNTs (I-SWNTs; Figure S2). In the first step, mild oxidation was used to modify and separate I-SWNT bundles into individual tl-SWNTs. This process has negligible effects on the average length of SWNTs (from 9.4 to 9.1 μm; Figure S3; Table S1). Raman spectroscopy shows the high ratio of the G and D peaks for tl-SWNTs ( $I_G/I_D = 34.6 \pm 4.0$ , reflecting intact structure and defects in SWNTs, respectively), indicating that the weak oxidation induces slight structural damage (Figure S4).42 In the second step, heterocyclic aramid chains were used to disperse tl-SWNTs in N,N-dimethylacetamide (DMAc; Figure S5). Transmission electron microscopy (TEM) and energy-dispersive spectroscopy images show the adsorption of heterocyclic aramid chains onto tl-SWNTs (Figures S6 and S7). Compared to I-SWNT dispersion, the significantly lower D90 value of tl-SWNT dispersion (from 0.71 to 0.41 μm) demonstrates the improved dispersion achieved through this two-step strategy (Figure S8; Note S1).

Next, we engineered heterocyclic aramid chains to improve their flexibility. Traditional heterocyclic aramid chains, polymerized from ternary monomers (*p*-phenylenediamine [PPD], 2-(4-aminophenyl)-1H-benzimidazol-5-amine [PABZ], and terephthaloyl chloride), exhibit relatively high rigidity, <sup>14,43</sup> limiting the draft ratio of fibers in the coagulation bath (≤2.4; Figures S9–S11). Such limitations hinder the alignment of tl-SWNTs within the fibers (Figure S12). To address this issue, flexible and asymmetric monomers (ODA) were introduced into traditional heterocyclic aramid chains. Our atomistic simulations show that the persistence lengths of heterocyclic aramid chains and ether-group heterocyclic aramid chains are 5.5 and 4.8 nm, respectively, supporting the improved flexibility of the engineered chains (Figure S13).

Subsequently, multi-stage drafting including the first-stage drafting in coagulation bath and the second-stage hot drafting was applied to fabricate the wet-spun fibers using spinning dope from the *in situ* polymerization of the SWNTs and heterocyclic aramid monomers (Figures S14–S18). Notably, the maximum enhancement efficiency of tl-SWNT on o-HAFs is observed at a PPD:ODA:PABZ molar ratio of 3:2:5, where tl-SWNT-o-HAFs exhibit peak values in both specific strength and specific toughness. Therefore, we selected the PPD:ODA: PABZ molar ratio of 3:2:5 for fiber preparation (Tables S3–S5). During the first-stage drafting in coagulation bath, the flexible ether-group heterocyclic aramid chains enable the fibers to

## **Matter** Article



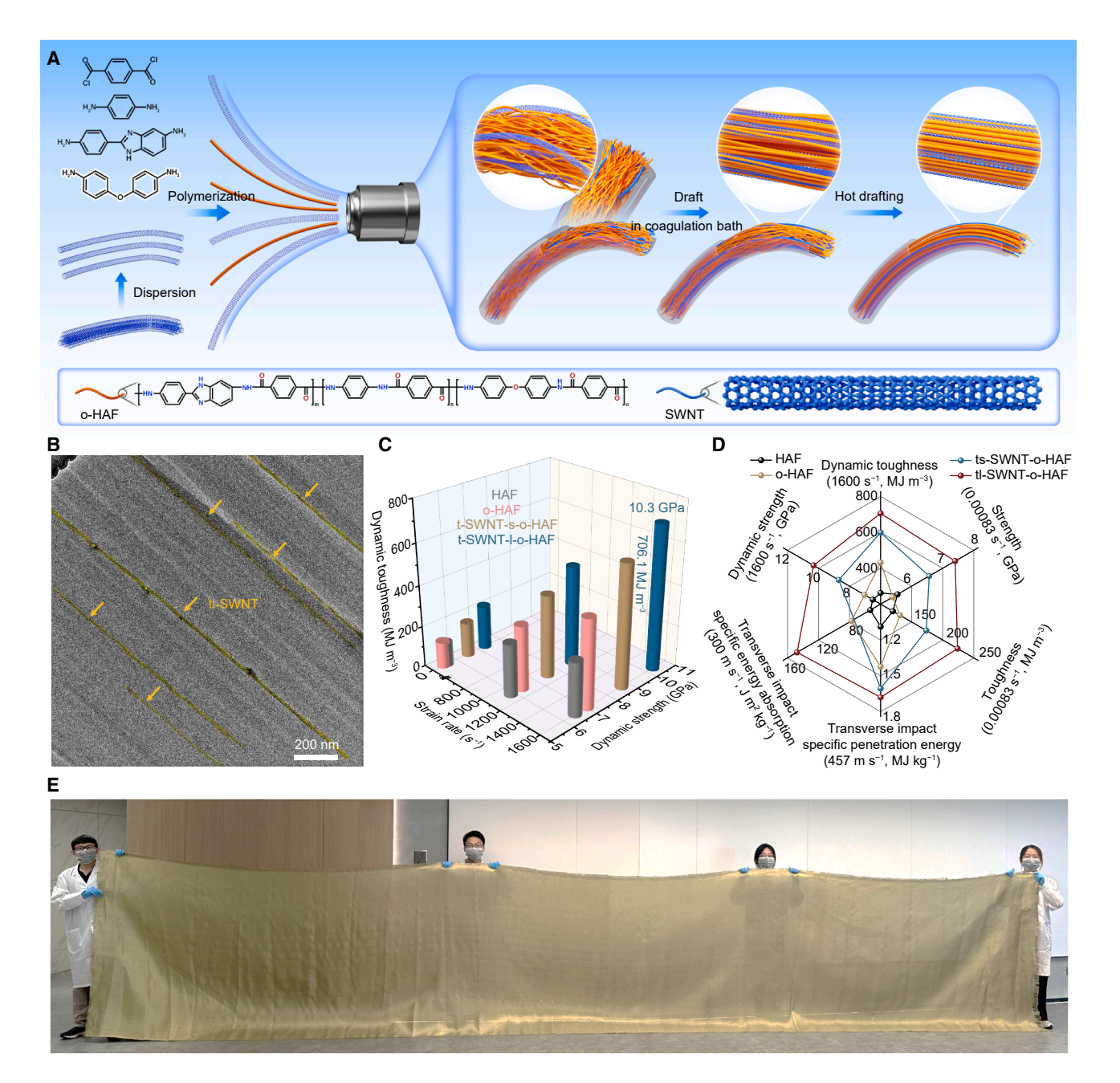


Figure 1. Preparation, structure, mechanical properties, and application of composite fibers

- (A) Schematic diagram of the preparation of composite fibers.
- (B) TEM image of aligned tl-SWNT within tl-SWNT-o-HAFs at a draft ratio of 2.8 in coagulation bath.
- (C) Comparison of the mechanical properties of fibers at different strain rates.
- (D) Radar chart for comparing the mechanical properties of different fibers.
- $\begin{tabular}{ll} \textbf{(E) Digital photograph of fabric woven from mass-produced tl-SWNT-o-HAFs}. \end{tabular}$

withstand a draft ratio of up to 3.0, exhibiting a 25% increase relative to traditional HAFs (Table S2). Upon multi-stage drafting, TEM images show that tl-SWNTs within tl-SWNT-o-HAFs change from bent to straight configurations as the draft ratio of the first-stage drafting in coagulation bath increases, indicating that the improved draft ratio is crucial for the alignment of tl-SWNTs (Figures 1B, 2A, and S19). Wide-angle X-ray scattering (WAXS)

analyses and mechanical tests show that the orientation degree and mechanical properties of ether-group HAFs (o-HAFs; "o" indicates the oxygen-containing ether group), o-HAFs composited with treated and short SWNTs (ts-SWNT-o-HAFs), and tl-SWNT-o-HAFs increase with draft ratios (Figures 2B and S20–S24; Note S2; Table S3). Among these fibers, the orientation degree and mechanical properties of tl-SWNT-o-HAFs improve



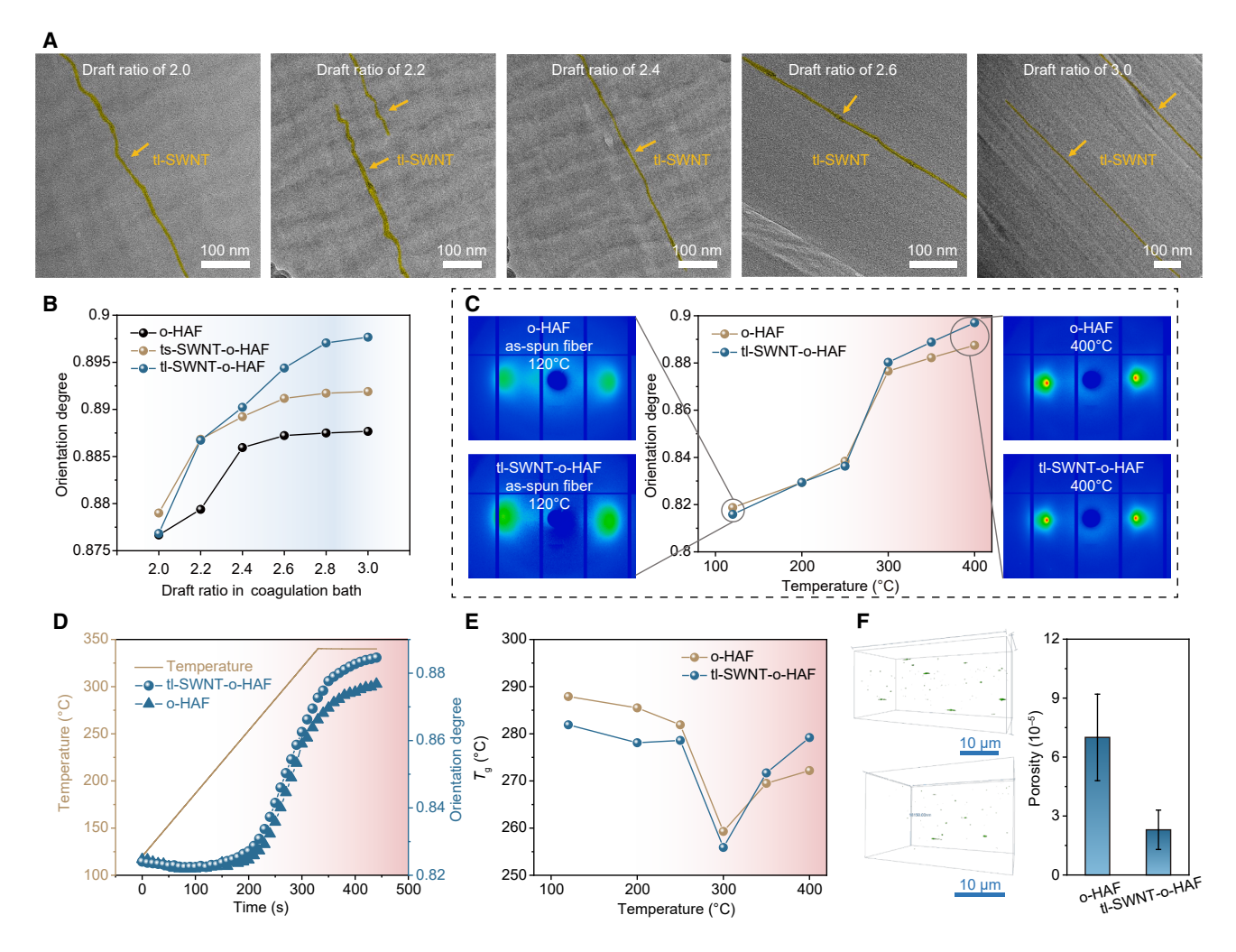


Figure 2. Structural characterization of composite fibers

- (A) TEM images of the arrangement for tl-SWNTs within tl-SWNT-o-HAFs with different draft ratios in coagulation bath.
- (B) Comparison of the orientation degree for fibers with different draft ratios.
- (C) Comparison of the orientation degree for o-HAFs and tl-SWNT-o-HAFs with different hot-drafting temperatures. The WAXS patterns on the left depict the as-spun fibers, while those on the right show the fibers with a hot-drafting temperature of 400°C.
- (D) Comparison of the orientation degree for o-HAFs and tl-SWNT-o-HAFs during in situ hot drafting.
- (E) Comparison of the glass transition temperature ( $T_g$ ) for o-HAFs and tl-SWNT-o-HAFs with different hot-drafting temperatures.
- (F) Three-dimensional void microstructures of o-HAFs (upper left) and ti-SWNT-o-HAFs (lower left); comparison of the porosities of o-HAFs and ti-SWNT-o-HAFs (right).

most rapidly and gradually reach the maximum values at a draft ratio of 2.8 in the coagulation bath (with specific strength increasing from 30.2  $\pm$  1.8 to 39.0  $\pm$  1.0 cN dtex $^{-1}$  and specific toughness from 61.4  $\pm$  4.6 to 88.0  $\pm$  2.3 J g $^{-1}$ ). These results indicate the effectiveness of multi-stage drafting on structural optimization and performance improvement of our fibers.

Interestingly, we found that the temperature during the second-stage hot drafting plays a crucial role in structural optimization and performance improvement. When the hot-drafting temperature is below 300°C, the orientation degree and performance of tl-SWNT-o-HAFs and o-HAFs are close (Figures 2C and S25–S28; Note S3; Tables S6 and S7). These results indicate that the addition of tl-SWNTs has a slight effect on the structure and performance of o-HAFs in this condition. In contrast, when the

hot-drafting temperature is above 300°C, the orientation degree and performance of tl-SWNT-o-HAFs are remarkably improved compared to o-HAFs. *In situ* hot-drafting experiment reveals that the orientation degree of tl-SWNT-o-HAFs increases more rapidly than that of o-HAFs above 300°C (Figures 2D and S29; Videos S1 and S2). This might be because the temperature (300°C) is higher than the glass transition temperature ( $T_g$ ) of tl-SWNT-o-HAFs (250°C–290°C; Figure 2E; Note S4). When the hot-drafting temperature is higher than the  $T_g$  of tl-SWNT-o-HAFs, the ether-group heterocyclic aramid chains become fluid. 35,44 Such a high fluidity would enable the aligned tl-SWNTs as templates to effectively promote polymer chain alignment around SWNTs, as well as reduce the porosity (from 0.007%  $\pm$  0.0022% to 0.0023%  $\pm$  0.001%; Figure 2F; Videos S3 and S4).

## **Matter** Article



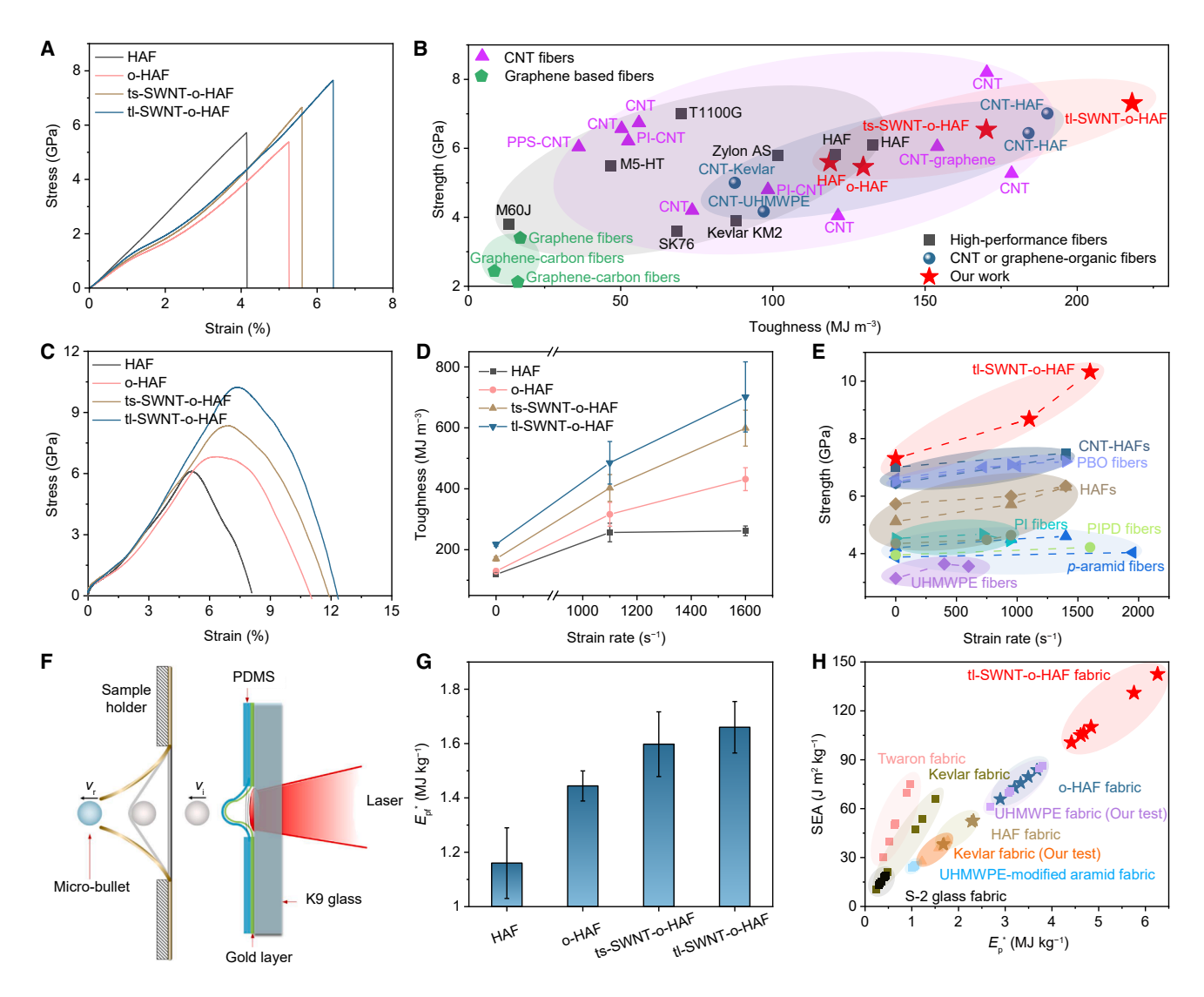


Figure 3. Performance and applications of composite fibers

- (A) Quasi-static stress-strain curves of different monofilament fibers.
- (B) Comparison of the strength and toughness for our fibers and other high-performance fibers.
- (C) Stress-strain curves of different fibers at a strain rate of about 1,600  $\rm s^{-1}$ .
- (D) Comparison of the toughness of fibers at different strain rates.
- (E) Comparison of the strength of our fibers and other polymer fibers at different strain rates.
- (F) Schematic diagram of laser-induced micro-ballistic impact tests on a monofilament fiber. PDMS,  $v_i$ , and  $v_r$  represent polydimethylsiloxane, impact velocity, and residual velocity, respectively.
- (G) Comparison of the specific penetration energy ( $E_{\rm pf}^{\star}$ ) of different fibers.
- (H) Comparison of SEA and the specific penetration energy  $(E_p^*)$  of different fabrics.

Finally, we compared the structures and mechanical properties of tl-SWNT-o-HAFs with those of other fibers (Figures S30–S35; Note S5; Tables S8–S11). The results show that tl-SWNT-o-HAFs (containing 0.075 wt % tl-SWNTs) exhibit the highest performance (Figures S36–S38). This enhancement stems from molecular engineering of building blocks combined with multistage drafting, where aligned tl-SWNTs effectively improve the orientation degree and reduce the porosity of composite fibers. Hence, we focus on the tl-SWNT-o-HAFs (containing 0.075 wt % tl-SWNTs) in the following discussion unless otherwise noted.

#### **Performance and applications**

The aligned tl-SWNTs and their optimized structure led to significant improvements in the quasi-static mechanical properties of both monofilament fibers and multifilament yarns. Compared to HAFs, tl-SWNT-o-HAF monofilament fibers exhibit a tensile strength of 7.3  $\pm$  0.1 GPa, a specific strength of 49.3  $\pm$  2.5 cN dtex $^{-1}$ , a toughness of 218.0  $\pm$  6.9 MJ m $^{-3}$ , and a specific toughness of 146.9  $\pm$  6.2 J g $^{-1}$ , which increase by 30.4%, 31.5%, 83.3%, and 84.3%, respectively (Figures 3A, S39, and S40; Tables S12 and S13). Notably, tl-SWNT-o-HAFs achieve the



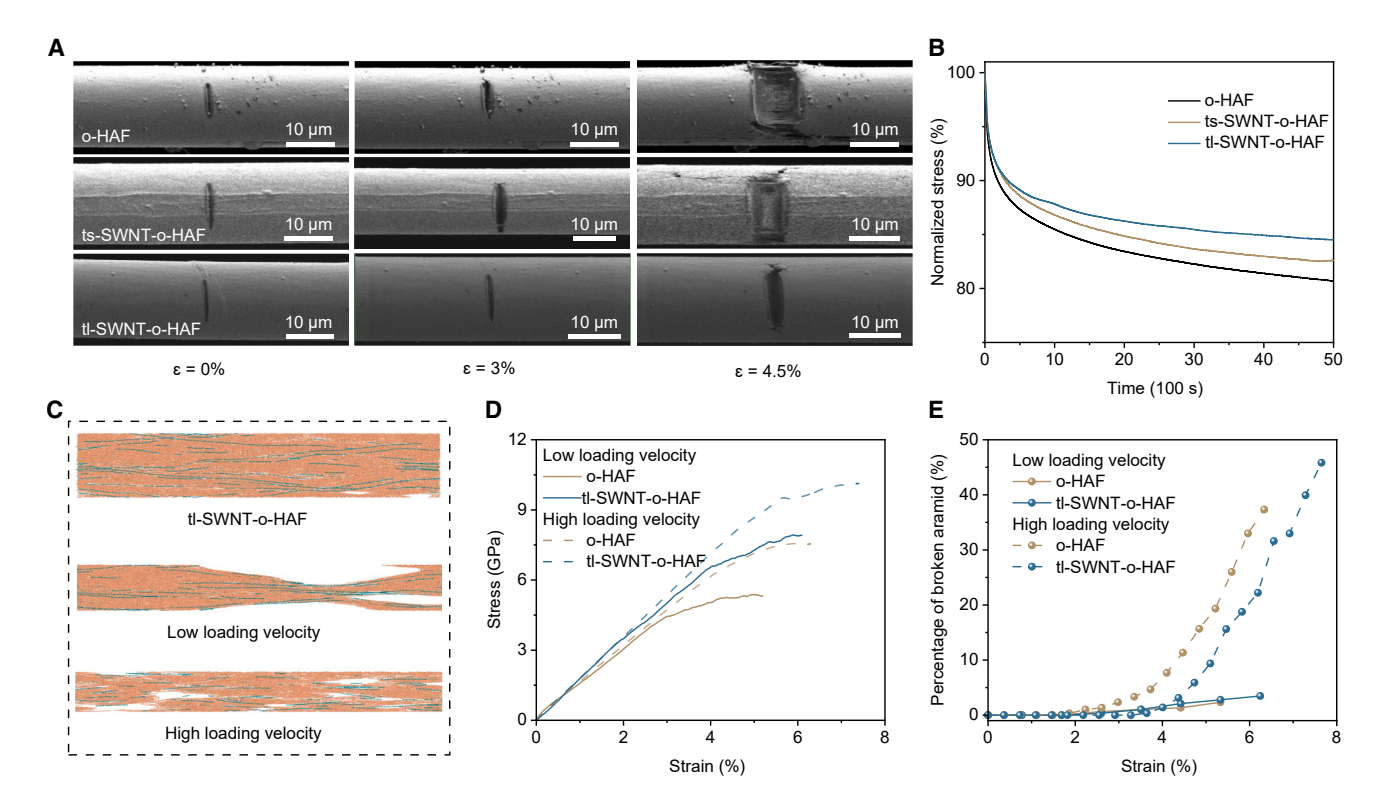


Figure 4. Strengthening mechanism of composite fibers

- (A) SEM images of cracks under different strains ( $\epsilon$ ).
- (B) Stress relaxation curves of different fibers at 1.5% strain.
- (C) Simulation snapshots of tl-SWNT-o-HAF under different loading velocities.
- (D) Stress-strain curves of fibers under different loading velocities.
- (E) Percentage of broken aramid chains for different fibers during tension.

highest toughness among all macroscopic fibers with strength exceeding 2 GPa, indicating the great potential for impact-protective applications (Figure 3B; Table S14). Compared to high-performance fibers reinforced by graphene and CNTs, tl-SWNT-o-HAFs exhibit the highest strength and toughness with a small addition of tl-SWNTs (Figure S41; Table S15). Multifilament yarns of tl-SWNT-o-HAFs also exhibit excellent specific strength, specific toughness, and elongation at break, compared to our prepared fibers and commercial high-performance fibers, such as aramid fibers, carbon fibers, poly(p-phenylene-2,6-benzobisoxazole) fibers, and UHMWPE fibers (Figures S42–S44; Table S16).

The dynamic behavior of fibers was evaluated by a mini-split Hopkinson tension bar (Figures S45 and S46). The results demonstrate that tl-SWNT-o-HAFs exhibit the highest dynamic strength and dynamic toughness among our prepared fibers (Figures 3C–3E and S47). Compared to quasi-static mechanical properties, tl-SWNT-o-HAFs exhibit a dynamic strength of 8.7  $\pm$  0.8 GPa and 10.3  $\pm$  0.6 GPa at strain rates of about 1,100 and 1,600 s $^{-1}$ , which increase by 19.2% and 41.1%, respectively. Similarly, dynamic toughness of 485.4  $\pm$  69.8 MJ m $^{-3}$  and 706.1  $\pm$  46.4 MJ m $^{-3}$  is achieved, corresponding to increases of 122.7% and 223.9%, respectively. This indicates an improvement in strengthening efficiency as the strain rate increases. The dynamic strength and dynamic toughness of tl-SWNT-o-HAFs at

a strain rate of 1,600 s<sup>-1</sup> are 1.6 and 2.7 times that of HAFs, respectively. The dynamic toughness surpasses all reported macroscopic fibers (Tables S17 and S18), Fracture morphology analysis shows that tl-SWNT-o-HAFs exhibit the most pronounced synergistic fracture and the mildest kink bond (Figures S48 and S49; Note S6). This indicates that tl-SWNT-o-HAFs possess strong interfacial interactions and high load transfer efficiency, which can inhibit the slippage of ether-group heterocyclic aramid chains during the tension. Notably, tl-SWNT-o-HAFs experience a ductile-to-brittle transition in the fracture mode under high-strain-rate loadings, which is beneficial to fiber performance under high-speed impact conditions (Note S7). Similarly, enhanced dynamic performance is also observed in multifilament yarns (Figure S50; Table S19). Under high-strain-rate loadings, the multifilament yarns tend to break simultaneously, suggesting a uniform deformation throughout the yarns (Figure S51). These behaviors ultimately contribute to enhanced mechanical properties, highlighting the great potential for high-speed impact-protective applications when woven into fabrics.

To directly evaluate the impact performance, laser-induced micro-ballistic impact tests were conducted (Figures 3F, S52, and S53). The micro-bullet (99.8  $\pm$  3.9  $\mu m$  in diameter) accurately impacts the monofilament fibers (about 16  $\mu m$  in diameter) at an average speed of about 457 m s $^{-1}$ . The specific penetration

## **Matter** Article



energy (SPE) for a monofilament fiber is  $E_{\rm pf}^*=\Delta E_{\rm k}/m_0=\Delta E_{\rm k}/\lambda d=m(v_{\rm i}^2-v_{\rm r}^2)/2\lambda d$ , where  $\Delta E_{\rm k}$  is kinetic energy loss of the micro-bullet,  $m_0$  is mass of target in the micro-bullet projected area,  $\lambda$  is linear density of fibers, and m, d,  $v_{\rm i}$ , and  $v_{\rm r}$  represent the mass, diameter, impact velocity, and residual velocity of the micro-bullet, respectively. Among these fibers, tl-SWNT-o-HAFs exhibit the highest  $E_{\rm pf}^*$ , reaching 1.66 MJ kg $^{-1}$  (Figure 3G; Table S20), which is attributed to the enhanced interfacial interactions and load transfer efficiency (Figure S54). The SPE of tl-SWNT-o-HAFs is actually underestimated due to the limited energy delocalization for the short-gauge monofilament ( $\sim$ 650  $\mu$ m),  $^{46-48}$  indicating the excellent energy absorption capacity under high-speed transverse impact (Note S8).

To demonstrate the practical application of composite fibers in impact protection, we wove the mass-produced tl-SWNT-o-HAFs into fabrics and conducted ballistic impact tests using 1.1 g standard fragments (Figures 1E and S55–S57). The SPE of fabrics is calculated as  $E_{\rm p}^* = \Delta E_{\rm k}/m_0 = m(v_{\rm i}^2-v_{\rm r}^2)/2A_{\rm c}A_{\rm s}$ , where  $A_{\rm d}$  and  $A_{\rm s}$  represent the areal density of fabrics and projected area of the fragment on fabrics, respectively. The traditional specific energy absorption (SEA =  $\Delta E_{\rm k}/A_{\rm d}$ ) of the fabric is also calculated to evaluate its ballistic impact performance. Compared to our other fabrics and commercial fabrics, tl-SWNT-o-HAF fabrics exhibit the highest SPE and SEA, demonstrating the excellent impact resistance of tl-SWNT-o-HAF at the macroscale (Figures 3H, S58, and S59; Table S21). This highlights their considerable potential as an ideal protective material in modern industries.

#### Strengthening mechanism

To understand the ultra-high dynamic performance of our fibers, we conducted multiscale analyses based on experimental evidence. The following analyses would show that the inhibited slippage and thus remarkable breakage of polymer chains are crucial for ultra-high dynamic performance, which is attributed to the improved alignment of polymer chains, reduced porosity. and thus enhanced interfacial interactions as well as load transfer efficiency within the fibers induced by tl-SWNT templates and multi-stage drafting. Regarding the alignment of polymer chains, WAXS experiments have demonstrated the increased alignment of polymer chains within tl-SWNT-o-HAFs as the draft ratio increases (Figures 2A and 2B). This is because the interfacial energy between the ether-group heterocyclic aramid chains and SWNTs (57.5 meV per atom) is higher than that between the ether-group heterocyclic aramid chains (21.6 meV per atom) and such a high interfacial energy would enable SWNTs as templates to promote polymer chain alignment around SWNTs during the multi-stage drafting.8 Regarding the porosity of our fibers, focused ion beam (FIB) and scanning electron microscopy (SEM) tomography (FIB-SEMT) experiments have shown that the porosity of tl-SWNT-o-HAFs is remarkably reduced compared to o-HAFs (Figure 2F). Consequently, the improved alignment and reduced porosity increase the interfacial interactions and load transfer efficiency. Furthermore, laterally pre-cracked fibers were axially stretched to track the mode I crack evolutions (Figures 4A, S60, and S61; Videos S5, S6, S7, and S8). The results show that the crack of tl-SWNT-o-HAFs exhibits minimal growth compared to o-HAFs and ts-SWNT-o-HAFs. Meanwhile, tl-SWNT-o-HAFs show the highest resistance to stress relaxation (Figure 4B). These results further support the improved interfacial interactions and load transfer efficiency within the tl-SWNT-o-HAFs.

Next, we explored the performance of the fibers using coarsegrained molecular dynamics simulations based on the experimental evidence. The simulations show that the slippage of aramid chains is remarkably inhibited for tl-SWNT-o-HAFs under the high loading velocity compared to that under the low loading velocity (Figures 4C, S62, and S63; Table S22). The tensile strength increases from 5.3 to 10.1 GPa for tl-SWNT-o-HAFs under low and high loading velocities (Figure 4D), which are generally consistent with the experimental measurements. To understand the macroscopic performance of fibers, we analyzed the microscopic behaviors of individual aramid chains within the fibers (Figure 4E). Under the low loading velocity, only 2% and 3% of aramid chains break for o-HAFs and tl-SWNT-o-HAFs, respectively. In contrast, under the high loading velocity, 37% and 46% of aramid chains break for o-HAFs and tl-SWNT-o-HAFs up to the peak stress, respectively. These simulations indicate the ductile-to-brittle transition in the fracture mode with the increase of loading velocity, which agrees with the ductile-to-brittle fracture morphologies as observed in highspeed experimental tests (Figures S50 and S54). More importantly, the breakage of these chains within tl-SWNT-o-HAFs occurs at the high loading level, indicating the relatively uniform deformation of such fibers. To summarize, the ultra-high dynamic performance of our fibers is attributed to the inhibited slippage and thus remarkable breakage of polymer chains, which originate from the improved alignment of polymer chains, reduced porosity, and thus enhanced interfacial interactions and load transfer efficiency.

#### **DISCUSSION**

The trade-off between strength and toughness is a persistent challenge in material science. Simultaneous breakthroughs of strength and toughness require innovative fabrication strategies. Our concept for fabricating high-strength and high-toughness aramid fibers is to utilize the high intrinsic mechanical performance of polymer chains by inhibiting their slippage at the microscale. In this work, we develop an effective strategy that regulates the orientation of I-SWNTs within fibers to inhibit chain slippage. I-SWNTs and aramid chains were molecularly engineered to achieve compatibility, while multi-stage drafting was designed for the alignment of both long SWNTs and aramid chains to enhance interfacial interactions and load transfer efficiency. Based on this strategy, we fabricated aramid fibers with a dynamic strength up to 10 GPa and dynamic toughness up to 700 MJ m<sup>-3</sup>. To the best of our knowledge, the dynamic toughness of our fibers surpasses those of all other commercial and non-commercial fibers tested under the same conditions. Fabrics woven from these mass-produced fibers also exhibit superior anti-ballistic impact performance, shedding light on the practical applications of these fibers.

Combining experimental evidence and atomistic simulations, the ultra-high performance is attributed to the inhibited slippage and thus remarkable breakage of polymer chains at high loading





levels. These mechanism insights significantly differ from the conventional failure mode dominated by chain slippage, offering a special perspective on the failure mechanisms of polymer fibers with ultra-high strength and ultra-high toughness. To summarize, our study not only presents an effective strategy for the fabrication of aramid fibers with ultra-high dynamic strength as well as the highest recorded dynamic toughness but also provides fresh mechanism insights.

#### **METHODS**

#### **Materials**

DMAc (≥99%) with water content less than 50 ppm, lithium chloride (LiCl, >99%), nitric acid (HNO<sub>3</sub>, 65%–68%), terephthaloyl chloride ([TPC] >99%), PPD (>99%), ODA (>99%), and PABZ (≥99.5%) were purchased from Beijing InnoChem Science and Technology Co., Ltd. SWNTs (>95%) were purchased from Jiangsu XFNANO Materials Tech Co., Ltd. All reagents were used as received without further purification.

#### **Modification of SWNTs**

The pristine I-SWNTs were initially purified by annealing in a muffle furnace at 400°C for 4 h to eliminate impurities. Next, the purified I-SWNTs (0.5 g) were dispersed in concentrated HNO<sub>3</sub> (65% w/w, 250 mL) by sonication for 1 h. Subsequently, the I-SWNTs-HNO3 mixture was refluxed at 140°C for 2 h with vigorous stirring to prepare tl-SWNTs. The resulting solution was then washed 4-5 times with deionized water through centrifugation at  $10,000 \times g$  for 15 min to remove the residual HNO<sub>3</sub> and impurities. The tl-SWNTs were subsequently dispersed in deionized water and further purified using dialysis to eliminate the remaining HNO3. The above solution was then subjected to sonication for 30 min in an ice-water bath using an ultrasonic cell disruption system (Scientz, JY99-IIDN) with 60% of the maximum power (1,500 W) to minimize agglomeration of tl-SWNTs. Finally, the solution was processed using a freeze dryer to obtain tl-SWNT powder. A similar procedure was employed to prepare the ts-SWNT powder from short SWNTs (s-SWNTs).

#### **Preparation of SWNT dispersion**

The tl-SWNT dispersion was prepared using a method assisted by heterocyclic aramid chains. Specifically, tl-SWNT powder (0.25 g) was added to a DMAc solution containing 3.5 wt % LiCl (200 mL) and sonicated with 60% of the maximum power (1,500 W) for 30 min in an ice-water bath using an ultrasonic cell disruption system. Subsequently, the heterocyclic aramid spinning dope (12.5 g, the mass of heterocyclic aramid chains is 0.5 g) was added to the above solution. Sonication was continued for 30 min and repeated 3 times with 30-min intervals between each session. The ts-SWNT, I-SWNT, and s-SWNT dispersions were prepared under the same procedures by dispersing ts-SWNT, I-SWNT, and s-SWNT powders, respectively.

## *In situ* synthesis of tl-SWNT/ether-group heterocyclic aramid spinning dope

The tl-SWNT/ether-group heterocyclic aramid spinning dope was prepared by a low-temperature polycondensation process

(Figure S14). First, the polymerization monomers ( $n_{PPD}$ : $n_{ODA}$ :  $n_{PABZ}$  = 3:2:5) were mixed into a DMAc solution containing 3.5 wt % LiCl and stirred for 30 min. Subsequently, an optimized amount of the tl-SWNT dispersion was added to the solution and stirred for 10 min. The weight percentage of tl-SWNTs was calculated based on the ratio of the tl-SWNT mass to the mass of the ether-group heterocyclic aramid after polymerization. After cooling the mixture to below 10°C, TPC was added, and the reaction proceeded under stirring for 2 h. After the reaction, a black viscous spinning dope with a dynamic viscosity ranging from 40,000 to 60,000 mPa·s was obtained (Figure S15). The content of tl-SWNT/ether-group heterocyclic aramid chains is 4 wt %. For comparison, the pure ether-group heterocyclic aramid spinning dope was obtained following a similar preparation procedure without adding the tl-SWNT dispersion. The pure heterocyclic aramid spinning dope was obtained following a similar preparation procedure without adding the tl-SWNT dispersion and ODA ( $n_{PPD}$ : $n_{PABZ} = 3:7$ ). The ts-SWNT/ethergroup heterocyclic aramid, I-SWNT/ether-group heterocyclic aramid, and s-SWNT/ether-group heterocyclic aramid spinning dopes were prepared under the same procedures by adding ts-SWNT, I-SWNT, and s-SWNT dispersion, respectively.

#### **Fabrication of tI-SWNT-o-HAFs**

The tl-SWNT-o-HAFs were prepared through multi-stage drafting (Figures S14 and S16). The obtained tl-SWNT/ether-group heterocyclic aramid spinning dope was poured into a degassing tank equipped with a metering pump and a nitrogen inlet. After a vacuum-defoaming treatment for 2 h, the spinning dope was transferred to a spinning pot on the spinning line. After extrusion by a spinning pump under high-pressure nitrogen, the spinning dope was transported to a spinneret plate and injected into multi-stage coagulation baths. The primary coagulation bath had a water to DMAc ratio of 1:1 at 25°C, while the secondary coagulation bath had a ratio of 4:1 at 40°C. The draft ratio in our discussion refers to the draft ratio in the secondary coagulation bath, which can reach a maximum of 3.0. The as-spun tl-SWNT-o-HAFs were obtained after washing with flowing deionized water and drying at 120°C. Then, the tl-SWNT-o-HAFs were obtained after the hot drafting in the N2 atmosphere at 400°C and collected using an automatic winding device (Figure S18). The spinning speed was about 4.0 m min<sup>-1</sup>. The o-HAFs, ts-SWNT-o-HAFs, I-SWNT-o-HAFs, and s-SWNT-o-HAFs were prepared under the same procedures by adding corresponding spinning dope. The as-spun o-HAFs were prepared under the same procedures as as-spun tl-SWNT-o-HAFs by adding the corresponding spinning dope. The HAFs were prepared under similar procedures by adding the corresponding spinning dope and adjusting the draft ratio in the coagulation bath with a maximum of 2.4.

#### WAXS tests under in situ hot drafting

WAXS tests under *in situ* hot drafting were performed at a beamline (BL10U1) of the Shanghai Synchrotron Radiation Facility, utilizing an *in situ* stretching and heating device (Linkam, 200 N). The X-ray wavelength was set to 0.1239 nm with a detector-sample distance of 126.7 mm. During the *in situ* heating experiment, the as-spun yarns were fixed in the *in situ* stretching device using





a clamp of 10 mm length, and a constant load of 0.2 N was applied to ensure that the yarns remained straight. The temperature was increased to 320°C at a heating rate of 40°C min<sup>-1</sup>.

#### SEM tests under in situ tension treatment

SEM tests under *in situ* tension treatment were performed using the AMBER X plasma FIB-SEM system (Tescan) and an *in situ* stretching device (Linkam, 200 N). Samples were prepared by adhering monofilament fibers to rectangular paper frames using epoxy resin glue with a gauge length of 2 mm. Prior to the *in situ* tension experiment, FIB was used to create small cracks with a length of approximately 5.0  $\mu$ m, a width of about 0.7  $\mu$ m, and a depth of around 0.5  $\mu$ m. During the *in situ* tension experiment, the tensile speed was set to 1 mm min<sup>-1</sup>, while the SEM images were collected at an accelerating voltage of 10 kV and videos were collected using screen recording software.

#### **Dynamic mechanical properties**

The dynamic mechanical properties of both monofilament fibers and multifilament yarns under high strain rates were measured using a developed mini-split Hopkinson tension bar (mini-SHTB; Figure S45). The fiber specimen was glued to a sample holder with a gauge length of 4.5 mm before being mounted onto the mini-SHTB. Prior to testing, the legs of the paper frame were carefully cut to release the sample. The sleeve-type projectile was launched using an air gun and impacted an energy-absorbing bar fixed at the end of the incident bar, generating a tensile stress wave. This wave propagated along the incident bar and reached the sample, causing the fiber fracture. The fracture force of the fiber was measured using a high-frequency quartz piezoelectric force sensor (Kistler 9001, 180 kHz). Due to the sufficiently high impact impedance of the incident bar, its loading end can be considered a free boundary condition compared to the fiber. As a result, the strain rate  $\dot{\varepsilon}(t)$ , strain  $\varepsilon(t)$ , and stress  $\sigma(t)$  of a single fiber at different time can be analyzed,3,8

$$\dot{\varepsilon}(t) = 2C_0 \frac{\varepsilon_1}{I_s}$$
 (Equation 1)

$$\varepsilon(t) = 2C_0 \int_0^t \frac{\varepsilon_1}{I_s} dt$$
 (Equation 2)

$$\sigma(t) = \frac{F}{A_s}$$
 (Equation 3)

where  $C_0$ ,  $I_s$ , and  $A_s$  are the elastic wave velocity of the incident bar, length, and cross-sectional area of the sample, respectively.  $\varepsilon_l$  and F are strain in the incident bar and force of the sample, respectively. In our previous work,  $^3$  the strain was corrected accordingly:

$$\varepsilon_{\text{Corrected}} = \frac{\Delta I - C_{\$}F}{I_0}$$
 (Equation 4)

where  $C_{\rm S}$  is the value of system compliance, which is determined as the intercept 0.0015 mm  $N^{-1}$  for the zero gauge length.

The typical engineering stress-strain and strain rate-strain curves of monofilament fiber are shown in Figure S46. When the fiber stress reaches its peak, it is under constant strain

rate loading. The dynamic strength is defined as the peak force recorded by the force sensor divided by the cross-sectional area. The toughness of the fiber is represented by the area enclosed by the stress-strain curve and the coordinate axis.

#### Laser-induced micro-ballistic impact tests

The specific penetration energy for monofilament fiber,  $E_{\rm pf}^{\star}$ , was measured by laser-induced micro-ballistic impact tests (Figure S52). In the experiment, high-pressure plasma was generated through the interaction of a focused pulsed laser with a 100-nm-thick gold film, under the constraint of 4-mm-thick K9 glass. This caused the 78-µm-thick polydimethylsiloxane (PDMS) film, in direct contact with the gold film, to expand rapidly. During this process, a polystyrene micro-bullet (99.8  $\pm$  3.9 µm in diameter) was accelerated and placed on the backside of the PDMS film, impacting the fiber at an average speed of about 457 m s $^{-1}$ , as measured by a high-speed camera (KIRANA UHS Camera) with an imaging rate of 5  $\times$  10 $^6$  fps, along with the SI-LUX640 automatic laser lighting system. Additionally, residual velocity was measured to assess the fiber's impact resistance.

#### **RESOURCE AVAILABILITY**

#### **Lead contact**

Further information and requests for resources and reagents should be directed to and will be fulfilled by the lead contact, Jin Zhang (jinzhang@pku.edu.cn).

#### Materials availability

Materials are available upon request from the lead contact, Jin Zhang.

#### **Data and code availability**

Data supporting the findings of this paper are available within the article and its supplemental information files and from the lead contact upon reasonable request.

#### **ACKNOWLEDGMENTS**

This work was supported by the Shenzhen Science and Technology Innovation Commission (5420100461 and 5420100821), the Ministry of Science and Technology of China (2022YFA1203304), the National Natural Science Foundation of China (22494642, 52403345, 52021006, 12272391, and 12232020), the Strategic Priority Research Program of CAS (XDB36030100), the Beijing Nova Program (20240484491), the China Postdoctoral Science Foundation (BX20250288, 2024M753316, and 2025M770096), the Postdoctoral Fellowship Program of CPSF (GZC20241782), the CAS Project for Young Scientists in Basic Research (YSBR-096), and the Beijing National Laboratory for Molecular Sciences (BNLMS-CXTD-202001). We thank the support from Guangdong Provincial Key Laboratory of Nano-Micro Materials Research. We also thank the staff members of BL19U2 and BL10U1 beamlines at Shanghai Synchrotron Radiation Facility (SSRF) for providing technical support and assistance in data collection and analysis. The numerical calculations reported in this work were performed on the supercomputing system in the Supercomputing Center of Wuhan University.

#### **AUTHOR CONTRIBUTIONS**

Conceptualization, J.Z., Z.G., K.J., J. Luo, M.L., X. Lei, and X.J.; methodology, J. Luo, M.L., X. Lei, X.J., D.Y., J. Li, Z.Z., H.D., C.L., W.Z., Z.H., X. Li, S.X., J.H., and L.T.; investigation, J. Luo, M.L., X. Lei, and X.J.; writing – original draft, J. Luo, M.L., X. Lei, and X.J.; writing – review & editing, J.Z., Z.G., K.J., E.G., X.W., and L.T.; funding acquisition, J.Z., Z.G., K.J., X. Lei, E.G., and X.W.;

Please cite this article in press as: Luo et al., Aramid fibers with dynamic strength up to 10 GPa and dynamic toughness up to 700 MJ m<sup>-3</sup>, Matter (2025), https://doi.org/10.1016/j.matt.2025.102496





resources, J.Z., Z.G., K.J., E.G., and X.W.; supervision, J.Z., Z.G., K.J., E.G., and X.W.

#### **DECLARATION OF INTERESTS**

The authors declare no competing interests.

#### SUPPLEMENTAL INFORMATION

Supplemental information can be found online at https://doi.org/10.1016/j.matt.2025.102496.

Received: May 23, 2025 Revised: August 22, 2025 Accepted: September 25, 2025

#### **REFERENCES**

- Eswarappa Prameela, S., Pollock, T.M., Raabe, D., Meyers, M.A., Aitkaliyeva, A., Chintersingh, K.-L., Cordero, Z.C., and Graham-Brady, L. (2022). Materials for extreme environments. Nat. Rev. Mater. 8, 81–88. https://doi.org/10.1038/s41578-022-00496-z.
- Xie, W., Zhang, R., Headrick, R.J., Taylor, L.W., Kooi, S., Pasquali, M., Müftü, S., and Lee, J.H. (2019). Dynamic strengthening of carbon nanotube fibers under extreme mechanical impulses. Nano Lett. 19, 3519– 3526. https://doi.org/10.1021/acs.nanolett.9b00350.
- Zhang, X., Lei, X., Jia, X., Sun, T., Luo, J., Xu, S., Li, L., Yan, D., Shao, Y., Yong, Z., et al. (2024). Carbon nanotube fibers with dynamic strength up to 14 GPa. Science 384, 1318–1323. https://doi.org/10.1126/science. adj1082.
- Ritchie, R.O. (2011). The conflicts between strength and toughness. Nat. Mater. 10, 817–822. https://doi.org/10.1038/nmat3115.
- Park, J.H., and Rutledge, G.C. (2017). 50th anniversary perspective: Advanced polymer fibers: High performance and ultrafine. Macromolecules 50, 5627–5642. https://doi.org/10.1021/acs.macromol.7b00864.
- Afshari, M., Sikkema, D.J., Lee, K., and Bogle, M. (2008). High performance fibers based on rigid and flexible polymers. Polym. Rev. 48, 230–274. https://doi.org/10.1080/15583720802020129.
- Cheng, C., Liao, X., Silva, J.M.d.S.E., Conceição, A.L.C., Carlos, D., Agarwal, S., Hou, H., Greiner, A., and Feng, W. (2024). Polymeric fibers with high strength and high toughness at extreme temperatures. Adv. Mater. 36, 2407712. https://doi.org/10.1002/adma.202407712.
- Luo, J., Wen, Y., Jia, X., Lei, X., Gao, Z., Jian, M., Xiao, Z., Li, L., Zhang, J., Li, T., et al. (2023). Fabricating strong and tough aramid fibers by small addition of carbon nanotubes. Nat. Commun. 14, 3019. https://doi.org/ 10.1038/s41467-023-38701-4.
- Chae, H.G., and Kumar, S. (2008). Making strong fibers. Science 319, 908–909. https://doi.org/10.1126/science.1153911.
- Richard, C., Bresson, B., Bès, M., Schittecatte, L., Le Roux, S., Didane, N., Bataille, F., Joannès, S., and Marcellan, A. (2023). Mechanisms of damage and fracture of aramid fibers: Focus on the role of microfibril cooperativity in fracture toughness. J. Polym. Sci. 61, 2549–2558. https://doi.org/10. 1002/pol.20230400.
- Yu, K., Li, C., Gu, W., Wang, M., Li, J., Wen, K., Xiao, Y., Liu, S., Liang, Y., Guo, W., et al. (2025). High-strength cellulose fibres enabled by molecular packing. Nat. Sustain. 8, 411–421. https://doi.org/10.1038/s41893-025-01523-x
- Liao, X., Dulle, M., de Souza e Silva, J.M., Wehrspohn, R.B., Agarwal, S., Förster, S., Hou, H., Smith, P., and Greiner, A. (2019). High strength in combination with high toughness in robust and sustainable polymeric materials. Science 366, 1376–1379. https://doi.org/10.1126/science. aay9033.

- Tikhonov, I.V., Tokarev, A.V., Shorin, S.V., Shchetinin, V.M., Chernykh, T.E., and Bova, V.G. (2013). Russian aramid fibres: past-present-future. Fibre Chem. 45, 1–8. https://doi.org/10.1007/s10692-013-9471-7.
- Xu, R., Qiu, Y., Tang, S., Yang, C., Dai, Y., Zhang, D., Gao, Y., Gao, K., Luo, L., and Liu, X. (2021). Preparation of high strength and toughness aramid fiber by introducing flexible asymmetric monomer to construct misplaced-nunchaku structure. Macromol. Mater. Eng. 306, 2000814. https://doi.org/10.1002/mame.202000814.
- Ding, X., Kong, H., Qiao, M., Hu, Z., and Yu, M. (2019). Study on crystallization behaviors and properties of F-III fibers during hot drawing in supercritical carbon dioxide. Polymers 11, 856. https://doi.org/10. 3390/polym11050856.
- Li, K., Luo, L., Huang, J., Wang, H., Feng, Y., and Liu, X. (2015). Enhancing mechanical properties of aromatic polyamide fibers containing benzimidazole units via temporarily suppressing hydrogen bonding and crystallization. J. Appl. Polym. Sci. 132, app.42482. https://doi.org/10.1002/app.42482.
- Yang, C., Wu, H., Dai, Y., Zhang, D., Xu, R., Luo, L., and Liu, X. (2020). Constructing mainstay-body structure in heterocyclic aramid fiber to simultaneously improve tensile strength and toughness. Compos. Part B-Eng. 202, 108411. https://doi.org/10.1016/j.compositesb.2020. 108411.
- Yang, C., Wu, H., Dai, Y., Tang, S., Luo, L., and Liu, X. (2019). Self-enhancement in aramid fiber by filling free hydrogen bonding interaction sites in macromolecular chains with its oligomer. Polymer 180, 121687. https://doi.org/10.1016/j.polymer.2019.121687.
- Lei, X., Xiao, K., Wu, X., and Huang, C. (2021). Dynamic mechanical properties of several high-performance single fibers. Materials 14, 3574. https://doi.org/10.3390/ma14133574.
- Yan, D., Luo, J., Wang, S., Han, X., Lei, X., Jiao, K., Wu, X., Qian, L., Zhang, X., Zhao, X., et al. (2024). Carbon nanotube-directed 7 GPa heterocyclic aramid fiber and its application in artificial muscles. Adv. Mater. 36, 2306129. https://doi.org/10.1002/adma.202306129.
- Peng, B., Locascio, M., Zapol, P., Li, S., Mielke, S.L., Schatz, G.C., and Espinosa, H.D. (2008). Measurements of near-ultimate strength for multiwalled carbon nanotubes and irradiation-induced crosslinking improvements. Nat. Nanotechnol. 3, 626–631. https://doi.org/10.1038/ nnano.2008.211.
- Bai, Y., Yue, H., Wang, J., Shen, B., Sun, S., Wang, S., Wang, H., Li, X., Xu, Z., Zhang, R., and Wei, F. (2020). Super-durable ultralong carbon nanotubes. Science 369, 1104–1106. https://doi.org/10.1126/science.aay5220.
- Chu, H., Hu, X., Wang, Z., Mu, J., Li, N., Zhou, X., Fang, S., Haines, C.S., Park, J.W., Qin, S., et al. (2021). Unipolar stroke, electroosmotic pump carbon nanotube yarn muscles. Science 371, 494–498. https://doi.org/ 10.1126/science.abc4538.
- Kinloch, I.A., Suhr, J., Lou, J., Young, R.J., and Ajayan, P.M. (2018). Composites with carbon nanotubes and graphene: An outlook. Science 362, 547–553. https://doi.org/10.1126/science.aat7439.
- Sun, X., Sun, H., Li, H., and Peng, H. (2013). Developing polymer composite materials: Carbon nanotubes or graphene? Adv. Mater. 25, 5153–5176. https://doi.org/10.1002/adma.201301926.
- Wen, Y., Jian, M., Huang, J., Luo, J., Qian, L., and Zhang, J. (2022). Carbonene fibers: Toward next-generation fiber materials. Nano Lett. 22, 6035–6047. https://doi.org/10.1021/acs.nanolett.1c04878.
- Punetha, V.D., Rana, S., Yoo, H.J., Chaurasia, A., McLeskey, J.T., Ramasamy, M.S., Sahoo, N.G., and Cho, J.W. (2017). Functionalization of carbon nanomaterials for advanced polymer nanocomposites: A comparison study between CNT and graphene. Prog. Polym. Sci. 67, 1–47. https://doi.org/10.1016/j.progpolymsci.2016.12.010.
- 28. Li, S., Feng, Y., Li, Y., Feng, W., and Yoshino, K. (2016). Transparent and flexible films of horizontally aligned carbon nanotube/polyimide

Please cite this article in press as: Luo et al., Aramid fibers with dynamic strength up to 10 GPa and dynamic toughness up to 700 MJ m<sup>-3</sup>, Matter (2025), https://doi.org/10.1016/j.matt.2025.102496

## **Matter** Article



- composites with highly anisotropic mechanical, thermal, and electrical properties. Carbon *109*, 131–140. https://doi.org/10.1016/j.carbon.2016. 07.052.
- Qin, M., Feng, Y., Ji, T., and Feng, W. (2016). Enhancement of cross-plane thermal conductivity and mechanical strength via vertical aligned carbon nanotube@graphite architecture. Carbon 104, 157–168. https://doi.org/ 10.1016/j.carbon.2016.04.001.
- Zhang, F., Ren, D., Huang, L., Zhang, Y., Sun, Y., Liu, D., Zhang, Q., Feng, W., and Zheng, Q. (2021). 3D interconnected conductive graphite nanoplatelet welded carbon nanotube networks for stretchable conductors. Adv. Funct. Mater. 31, 2107082. https://doi.org/10.1002/ adfm.202107082.
- Wu, Z., Zhao, Y., Yang, K., Guan, J., Wang, S., Gu, Y., Li, M., Feng, Y., Feng, W., and Ritchie, R.O. (2023). Enhancing the mechanical performance of fiber-reinforced polymer composites using carbon nanotubes as an effective nano-phase reinforcement. Adv. Mater. Interfac. 10, 2201935. https://doi.org/10.1002/admi.202201935.
- Coleman, J.N., Khan, U., Blau, W.J., and Gun'ko, Y.K. (2006). Small but strong: A review of the mechanical properties of carbon nanotube– polymer composites. Carbon 44, 1624–1652. https://doi.org/10.1016/j. carbon.2006.02.038.
- Qian, D., Dickey, E.C., Andrews, R., and Rantell, T. (2000). Load transfer and deformation mechanisms in carbon nanotube-polystyrene composites. Appl. Phys. Lett. 76, 2868–2870. https://doi.org/10.1063/1.126500.
- Zhang, W., Picu, R.C., and Koratkar, N. (2007). Suppression of fatigue crack growth in carbon nanotube composites. Appl. Phys. Lett. 91, 193109. https://doi.org/10.1063/1.2809457.
- Liu, Y., and Kumar, S. (2014). Polymer/carbon nanotube nano composite fibers–A review. ACS Appl. Mater. Interfaces 6, 6069–6087. https://doi. org/10.1021/am405136s.
- O'Connor, I., Hayden, H., Coleman, J.N., and Gun'ko, Y.K. (2009). Highstrength, high-toughness composite fibers by swelling Kevlar in nanotube suspensions. Small 5, 466–469. https://doi.org/10.1002/smll.200801102.
- Kumar, S., Dang, T.D., Arnold, F.E., Bhattacharyya, A.R., Min, B.G., Zhang, X., Vaia, R.A., Park, C., Adams, W.W., Hauge, R.H., et al. (2002). Synthesis, structure, and properties of PBO/SWNT composites. Macromolecules 35, 9039–9043. https://doi.org/10.1021/ma0205055.

- Ruan, S., Gao, P., and Yu, T.X. (2006). Ultra-strong gel-spun UHMWPE fibers reinforced using multiwalled carbon nanotubes. Polymer 47, 1604– 1611. https://doi.org/10.1016/j.polymer.2006.01.020.
- Papageorgiou, D.G., Li, Z., Liu, M., Kinloch, I.A., and Young, R.J. (2020).
  Mechanisms of mechanical reinforcement by graphene and carbon nanotubes in polymer nanocomposites. Nanoscale 12, 2228–2267. https://doi.org/10.1039/c9nr06952f.
- Sano, M., Kamino, A., Okamura, J., and Shinkai, S. (2001). Ring closure of carbon nanotubes. Science 293, 1299–1301. https://doi.org/10.1126/science.1061050.
- Mittal, G., Dhand, V., Rhee, K.Y., Park, S.J., and Lee, W.R. (2015). A review on carbon nanotubes and graphene as fillers in reinforced polymer nanocomposites. J. Ind. Eng. Chem. 21, 11–25. https://doi.org/10.1016/j.jiec. 2014.03.022.
- Zhang, S., Kang, L., Wang, X., Tong, L., Yang, L., Wang, Z., Qi, K., Deng, S., Li, Q., Bai, X., et al. (2017). Arrays of horizontal carbon nanotubes of controlled chirality grown using designed catalysts. Nature *543*, 234–238. https://doi.org/10.1038/nature21051.
- He, A., Xing, T., Liang, Z., Luo, Y., Zhang, Y., Wang, M., Huang, Z., Bai, J., Wu, L., Shi, Z., et al. (2023). Advanced aramid fibrous materials: Fundamentals, advances, and beyond. Adv. Fiber Mater. 6, 3–35. https://doi.org/10.1007/s42765-023-00332-1.
- Paul, D.R., and Robeson, L.M. (2008). Polymer nanotechnology: Nanocomposites. Polymer 49, 3187–3204. https://doi.org/10.1016/j.polymer. 2008.04.017.
- Lee, J.H., Loya, P.E., Lou, J., and Thomas, E.L. (2014). Dynamic mechanical behavior of multilayer graphene via supersonic projectile penetration. Science 346, 1092–1096. https://doi.org/10.1126/science.1258544.
- Hyon, J., Lawal, O., Thevamaran, R., Song, Y.E., and Thomas, E.L. (2021).
  Extreme energy dissipation via material evolution in carbon nanotube mats. Adv. Sci. 8, 2003142. https://doi.org/10.1002/advs.202003142.
- Xiao, K., Wu, X., Sang, Z., Subramanian, V., and Thomas, E.L. (2024). Load sharing and accumulated bond fracture in ion-irradiated carbon mat for energy dissipation. Sci. Adv. 10, eadq3805. https://doi.org/10.1126/ sciadv.adq3805.
- Portela, C.M., Edwards, B.W., Veysset, D., Sun, Y., Nelson, K.A., Kochmann, D.M., and Greer, J.R. (2021). Supersonic impact resilience of nanoarchitected carbon. Nat. Mater. 20, 1491–1497. https://doi.org/10.1038/s41563-021-01033-z.